DYNAMIC MODELING AND PARAMETRIC ANALYSIS OF DIFFERENTIAL GEARBOX USED IN ELECTRIC VEHICLE

Najeeb Ullah, Chaosheng Song, Caichao Zhu, Zhuxiang Ou, Cong Tan

The State Key Laboratory of Mechanical Transmissions, Chongqing University, Chongqing, China

e-mail: chaoshengsong@hotmail.com

The aim of this study is to perform the modeling and parametric analysis of dynamic mesh force in the light of resonance modes. Firstly, dynamic modeling of a differential gearbox has been performed by using the lumped parameter method. Then, the resonant points from Campbell diagrams were studied for the first three critical harmonic orders. Furthermore, two case studies were proposed in order to investigate the impact of radial clearance and face width on the dynamic mesh force along with resonance. Simultaneously, resonance identification and elimination were studied for two working conditions. Results show that the influence of lowering face width of pinions is more effective on mesh force reduction and resonance elimination as opposed to the first case study by enhancing wheel side mesh stiffness.

Keywords: electric vehicle, differential gearbox, dynamic mesh force, Campbell diagram, mode shapes

1. Introduction

It is an irrefutable fact that most vibration problems are associated with the resonance phenomenon, and this resonance point appears when dynamic forces in a machine stimulate natural frequencies in the surrounding structures. In addition, identification and elimination of resonance problems for different critical speeds is becoming more prominent due to increasing demand of vibration reduction in electric vehicles. Furthermore, differential gearbox of an electric vehicle used in this study has a very high input speed and is directly linked with the motor. Due to these reasons, modeling, design and mesh force parametric analysis of the differential gearbox were necessary to gain better understanding of the varying dynamics of the geared coupled system.

A large number of scholars have focused on the dynamics of geared rotor systems (Chen *et al.*, 2019; Liu *et al.*, 2019). In addition, natural frequencies were obtained by using an induction method in this study (Wu *et al.*, 2018). Investigation of a planetary gearbox casing in ANSYS was performed using modal analysis and mode shapes of the system were studied in (Walunj *et al.*, 2015). The study performed in (Kumar and Patil, 2016) depicted the weight calculation and modal analysis of the gearbox housing by taking into account different materials. Since the gearbox structure can be influenced by the gear mesh frequency and its harmonics so an analytical method was presented using vibration response analysis in order to predict the gearbox noise and vibration (Abouel-Seoud *et al.*, 2013). The modal analysis using a lumped parameter method and kinetic as well as strain energies of the gearbox transmission system used in a bucket wheel excavator were studied in (Karray *et al.*, 2017). A coupled marine gearbox model was built by using truss, spring and tetrahedral elements. Then the natural frequencies of the gearbox were compared with those obtained from experimental results (Liu *et al.*, 2014). Modal analysis of the gearbox for reduction of noise and vibration was performed thereby using the finite element method. However, detailed analysis of the Campbell diagram and mode shapes

was ignored (Chavan *et al.*, 2013; Nengquan *et al.*, 2011; Yu *et al.*, 2013). Later on, the modal analysis of a helical gear pair using different helix angle and transmission ratios was conducted by Korka and Gillich (2017).

Variations of different modal frequencies are analyzed and deformation shapes of wind turbine gearboxes by considering the impact of gear and bearing mesh stiffness are studied. The findings in this study are useful in obtaining modal characteristics and monitoring the faults in a gearbox (Yi *et al.*, 2016). Also the use of state space models and stabilization diagrams are equally important to investigate structural modes of machinery. So the Kalman filter method was used to compute the modal contribution for a time invariant damped system (Cara *et al.*, 2013). A comparison was made between strain and typical experimental modal analysis for the recognition of modal parameters of a structure. In addition, the accuracy level was analyzed for different structures using both techniques (Kranjc *et al.*, 2016). The importance of high speed machining can not be ignored due to its role in production and reduction of manufacturing costs. Therefore, several researchers worked on identification strategies on the basis of operational modal analysis for machine tools during machining conditions (Li *et al.*, 2013; Maamar *et al.*, 2017). Root cause inspection was studied for breakage on blades of a motor fan while mode shapes and natural frequencies were also investigated by developing a finite element model (Zhou *et al.*, 2017). A precise and estimated formulations for scaling mode shapes in modal analysis were presented and a detailed study was done in order to validate formulations on a plate model (López-Aenlle *et al.*, 2012). Experimental modal analysis was performed for a machine tool spindle system and modal parameters were proved by complex mode functions (Guo *et al.*, 2015). In short, there has been a lot of studies on modal analysis but the case studies for resonance elimination by focusing on dynamic mesh force analysis of machinery is very rare.

This paper conducts combination of the modeling and the dynamic mesh force analysis by considering critical resonance points in the Campbell diagram. Firstly, the dynamic modeling is performed by considering the dynamic transmission error. Then, the dynamic mesh force is gained and resonant modes are located. After that, the parametric study is performed for the dynamic mesh force analysis in such a way that two case studies are evaluated by using radial clearance of bearings and face width of pinions. The conducted case studies were never disclosed in the previous works, and the analysis results can be beneficial not only for altering mode locations of the dynamic mesh force but also for resonance and vibration reduction in a unique pattern of gearboxes.

2.   Dynamic modeling of differential gearbox

All gears in a differential gearbox are modeled as rigid disks while shaft mass and inertia are lumped at the gears. Due to complexity of the geared transmission system, the whole gearbox is mainly divided into the higher, middle and bevel differential or lower stage. The four degrees of freedom, three translational and one rotational with x_i, y_i, z_i and θ_i around the axis are considered for each gear, where $(i = 1, 2, \ldots, 8)$ depending upon gears of the coupled system. Hence, the total degrees of freedom will be 32 for the whole differential gearbox system. β_{ba} and β_{bb} stand for helix angle of base circles of the higher and middle stages, respectively. Whereas α_a, α_b and α_c denote pressure angle for gears of the higher, middle and lower stages, respectively. r_{bi}, m_i and I_i $(i = 1, 2, \ldots, 8)$ present base radius, mass and moment of inertia for the corresponding gears. T_m, T_{l1}, T_{12} stand for input torque on the higher stage, loaded torque on the left and right side of the lower stage, respectively. k_{ij} and c_{ij} are mesh stiffness and damping, where $(ij) = (1, 2, \ldots, 8)$ varies according to the corresponding gear pairs. δ_i presents reference cone angles for the corresponding gears of the lower or bevel differential stage, where $(i = 5, 6, 7, 8)$. Furthermore, E_{4r} stands for mounting radius of the wheel of the middle stage. l_{ij} is for dynamic

transmission error, where $(i = 1, 3, 5, 6)$ and $j = (2, 4, 7, 8)$ present corresponding gears. For the pinion of the higher stage, we have

$$
\begin{aligned}
&m_1\ddot{x}_1 + k_{b1x}x_1 + c_{b1x}\dot{x}_1 + (k_{12}l_{12} + c_{12}\dot{l}_{12})\cos\alpha_a\cos\beta_{ba} = 0 \\
&m_1\ddot{y}_1 + k_{b1y}y_1 + c_{b1y}\dot{y}_1 - (k_{12}l_{12} + c_{12}\dot{l}_{12})\sin\alpha_a\cos\beta_{ba} = 0 \\
&m_1\ddot{z}_1 + k_{b1z}z_1 + c_{b1z}\dot{z}_1 - (k_{12}l_{12} + c_{12}\dot{l}_{12})\sin\beta_{ba} = 0 \\
&I_1\ddot{\theta}_1 + (k_{12}l_{12} + c_{12}\dot{l}_{12})r_{b1}\cos\beta_{ba} = T_m
\end{aligned}
\tag{2.1}
$$

For the wheel of the higher stage

$$
\begin{aligned}
&m_2\ddot{x}_2 + k_{b2x}x_2 + c_{b2x}\dot{x}_2 - (k_{12}l_{12} + c_{12}\dot{l}_{12})\cos\alpha_a\cos\beta_{ba} = 0 \\
&m_2\ddot{y}_2 + k_{b2y}y_2 + c_{b2y}\dot{y}_2 + (k_{12}l_{12} + c_{12}\dot{l}_{12})\sin\alpha_a\cos\beta_{ba} = 0 \\
&m_2\ddot{z}_2 + k_{b2z}z_2 + c_{b2z}\dot{z}_2 + (k_{12}l_{12} + c_{12}\dot{l}_{12})\sin\beta_{ba} = 0 \\
&I_2\ddot{\theta}_2 + (k_{12}l_{12} + c_{12}\dot{l}_{12})r_{b2}\cos\beta_{ba} = 0
\end{aligned}
\tag{2.2}
$$

For the pinion of the middle stage

$$
\begin{aligned}
&m_3\ddot{x}_3 + k_{b3x}x_3 + c_{b3x}\dot{x}_3 - (k_{34}l_{34} + c_{34}\dot{l}_{34})\cos\alpha_b\cos\beta_{bb} = 0 \\
&m_3\ddot{y}_3 + k_{b3y}y_3 + c_{b3y}\dot{y}_3 - (k_{34}l_{34} + c_{34}\dot{l}_{34})\sin\alpha_b\cos\beta_{bb} = 0 \\
&m_3\ddot{z}_3 + k_{b3z}z_3 + c_{b3z}\dot{z}_3 - (k_{34}l_{34} + c_{34}\dot{l}_{34})\sin\beta_{bb} = 0 \\
&I_3\ddot{\theta}_3 - (k_{34}l_{34} + c_{34}\dot{l}_{34})r_{b3}\cos\beta_{bb} + k_{23\theta}(\theta_3 - \theta_4) + c_{23\theta}(\dot{\theta}_3 - \dot{\theta}_4) = 0
\end{aligned}
\tag{2.3}
$$

For the wheel of the middle stage

$$
\begin{aligned}
&m_4\ddot{x}_4 + k_{b4x}x_4 + c_{b4x}\dot{x}_4 + (k_{34}l_{34} + c_{34}\dot{l}_{34})\cos\alpha_b\cos\beta_{bb} - k_{54x}l_{54x} - k_{64x}l_{64x} = 0 \\
&m_4\ddot{y}_4 + k_{b4y}y_4 + c_{b4y}\dot{y}_4 + (k_{34}l_{34} + c_{34}\dot{l}_{34})\sin\alpha_b\cos\beta_{bb} + k_{54z}l_{54z} - k_{64z}l_{64z} = 0 \\
&m_4\ddot{z}_4 + k_{b4z}z_4 + c_{b4z}\dot{z}_4 + (k_{34}l_{34} + c_{34}\dot{l}_{34})\sin\beta_{bb} - k_{54y}l_{54y} + k_{64y}l_{64y} = 0 \\
&I_4\ddot{\theta}_4 - (k_{34}l_{34} + c_{34}\dot{l}_{34})r_{b4}\cos\beta_{bb} + k_{54x}\theta_4 E_{4r} - k_{64x}\theta_4 E_{4r} + k_{23\theta}(\theta_4 - \theta_3) \\
&\qquad + c_{23\theta}(\dot{\theta}_4 - \dot{\theta}_3) = 0
\end{aligned}
\tag{2.4}
$$

For the upper planet of the bevel differential assembly

$$
\begin{aligned}
&m_5\ddot{x}_5 + k_{54x}l_{54x} + c_{54x}\dot{l}_{54x} + (k_{57}l_{57} + c_{57}\dot{l}_{57})\cos\alpha_c - (k_{58}l_{58} + c_{58}\dot{l}_{58})\cos\alpha_c = 0 \\
&m_5\ddot{y}_5 + k_{54y}l_{54y} + c_{54y}\dot{l}_{54y} + (k_{57}l_{57} + c_{57}\dot{l}_{57})\cos\delta_5\sin\alpha_c \\
&\qquad - (k_{58}l_{58} + c_{58}x\dot{l}_{58})\cos\delta_5\sin\alpha_c = 0 \\
&m_5\ddot{z}_5 + k_{54z}l_{54z} + c_{54z}\dot{l}_{54z} + (k_{57}l_{57} + c_{57}\dot{l}_{57})\sin\delta_5\sin\alpha_c \\
&\qquad + (k_{58}l_{58} + c_{58}\dot{l}_{58})\cos\delta_5\sin\alpha_c = 0 \\
&I_5\ddot{\theta}_5 - (k_{57}l_{57} + c_{57}\dot{l}_{57})r_{b5}\cos\alpha_c - (k_{58}l_{58} + c_{58}\dot{l}_{58})r_{b5}\cos\alpha_c = 0
\end{aligned}
\tag{2.5}
$$

For the lower planet of the bevel differential assembly

$$
\begin{aligned}
&m_6\ddot{x}_6 + k_{64x}l_{64x} + c_{64x}\dot{l}_{64x} - (k_{67}l_{67} + c_{67}\dot{l}_{67})\cos\alpha_c + (k_{68}l_{68} + c_{68}\dot{l}_{68})\cos\alpha_c = 0 \\
&m_6\ddot{y}_6 + k_{64y}l_{64y} + c_{64y}\dot{l}_{64y} - (k_{67}l_{67} + c_{67}\dot{l}_{67})\cos\delta_6\sin\alpha_c \\
&\qquad + (k_{68}l_{68} + c_{68}\dot{l}_{68})\cos\delta_6\sin\alpha_c = 0 \\
&m_6\ddot{z}_6 + k_{64z}l_{64z} + c_{64z}\dot{l}_{64z} + (k_{67}l_{67} + c_{67}\dot{l}_{67})\sin\delta_6\sin\alpha_c \\
&\qquad + (k_{68}l_{68} + c_{68}\dot{l}_{68})\sin\delta_6\sin\alpha_c = 0 \\
&I_6\ddot{\theta}_6 - (k_{67}l_{67} + c_{67}\dot{l}_{67})r_{b6}\cos\alpha_c - (k_{68}l_{68} + c_{68}\dot{l}_{68})r_{b6}\cos\alpha_c = 0
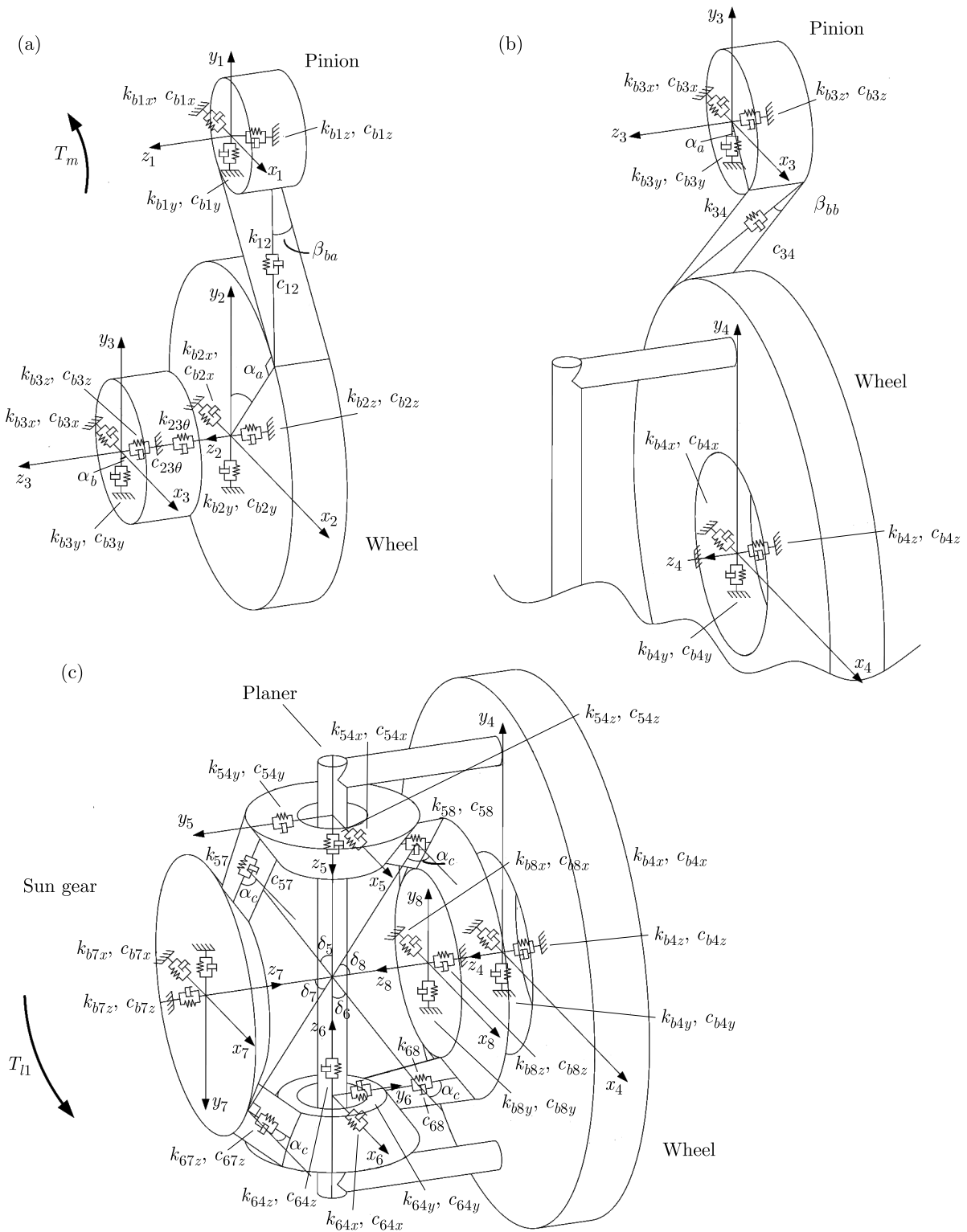\end{aligned}
\tag{2.6}
$$

Fig. 1. Dynamic model for the differential gearbox: (a) higher stage, (b) middle stage, (c) bevel differential assembly or lower stage

For the left sun gear of the bevel differential assembly

$$m_7\ddot{x}_7 + k_{b7x}x_7 + c_{b7x}\dot{x}_7 - (k_{57}l_{57} + c_{57}\dot{l}_{57})\cos\alpha_c + (k_{67}l_{67} + c_{67}\dot{l}_{67})\cos\alpha_c = 0$$
$$m_7\ddot{y}_7 + k_{b7y}y_7 + c_{b7y}\dot{y}_7 - (k_{57}l_{57} + c_{57}\dot{l}_{57})\cos\delta_7\sin\alpha_c$$
$$+ (k_{67}l_{67} + c_{67}\dot{l}_{67})\cos\delta_7\sin\alpha_c = 0$$
$$m_7\ddot{z}_7 + k_{b7z}z_7 + c_{b7z}\dot{z}_7 + (k_{57}l_{57} + c_{57}\dot{l}_{57})\sin\delta_7\sin\alpha_c$$
$$+ (k_{67}l_{67} + c_{67}\dot{l}_{67})\sin\delta_7\sin\alpha_c = 0$$
$$I_7\ddot{\theta}_7 - (k_{57}l_{57} + c_{57}\dot{l}_{57})r_{b7}\cos\alpha_c - (k_{67}l_{67} + c_{67}\dot{l}_{67})r_{b7}\cos\alpha_c = T_{11}$$

(2.7)

For the right sun gear of the bevel differential assembly

$$m_8\ddot{x}_8 + k_{b8x}x_8 + c_{b8x}\dot{x}_8 + (k_{58}l_{58} + c_{58}\dot{l}_{58})\cos\alpha_c - (k_{68}l_{68} + c_{68}\dot{l}_{68})\cos\alpha_c = 0$$
$$m_8\ddot{y}_8 + k_{b8y}y_8 + c_{b8y}\dot{y}_8 + (k_{58}l_{58} + c_{58}\dot{l}_{58})\cos\delta_8\sin\alpha_c$$
$$- (k_{68}l_{68} + c_{68}\dot{l}_{68})\cos\delta_8\sin\alpha_c = 0$$
$$m_8\ddot{z}_8 + k_{b8z}z_8 + c_{b8z}\dot{z}_8 + (k_{58}l_{58} + c_{58}\dot{l}_{58})\sin\delta_8\sin\alpha_c$$
$$+ (k_{68}l_{68} + c_{68}\dot{l}_{68})\sin\delta_8\sin\alpha_c = 0$$
$$I_8\ddot{\theta}_8 - (k_{58}l_{58} + c_{58}\dot{l}_{58})r_{b8}\cos\alpha_c - (k_{68}l_{68} + c_{68}\dot{l}_{68})r_{b8}\cos\alpha_c = T_{12}$$

(2.8)

where l_{12} is dynamic transmission error between the pinion and wheel of the higher stage; l_{34} is dynamic transmission error for the pinion and wheel of the middle stage. l_{57} shows dynamic transmission error for the upper planet and the left sun; while l_{58} is dynamic transmission error between the upper planet and the right sun. In the same way, l_{67} is dynamic transmission error between the left sun and the lower planet. Whereas, l_{68} denotes dynamic transmission error between the right sun and the lower planet. $[l_{54x}, l_{54y}, l_{54z}]^{\mathrm{T}}$ shows relative displacement between the upper planet and wheel of the middle stage, while $[l_{64x}, l_{64y}, l_{64z}]^{\mathrm{T}}$ is for relative displacement between the lower planet and wheel of the middle stage. The above equations are organized and expressed using Lagrange's method whose general dynamic equation of the system is as follows

$$\mathbf{M}\ddot{\mathbf{q}} + \mathbf{C}\dot{\mathbf{q}} + \mathbf{K}\mathbf{q} = \mathbf{Q} \tag{2.9}$$

where $\mathbf{M}$, $\mathbf{C}$, $\mathbf{K}$ and $\mathbf{Q}$ represent the mass, damping, stiffness and excitation matrix, respectively. $\mathbf{q}$ is the coordinate matrix of the coupled system, which is given as

$$\mathbf{q} = [x_1, y_1, z_1, \theta_1, x_2, y_2, z_2, \theta_2, x_3, y_3, z_3, \theta_3, x_4, y_4, z_4, \theta_4, x_5, y_5, z_5, \theta_5,$$
$$x_6, y_6, z_6, \theta_6, x_7, y_7, z_7, \theta_7, x_8, y_8, z_8, \theta_8]$$

(2.10)

3. Transmission principle analysis of the differential gearbox

According to the detailed parameters of gears, shafts and bearings, the dynamic model has been built in MASTA, which is shown in Fig. 2. Whereas, Table 1 and 2 present all the basic geometrical parameters of the differential gearbox. The working principle of the actual gearbox used in this study can be explained in such a way that it has an input rotational speed of 6000--12000 rpm and is made for the higher stage, middle stage and lower stage. The input power is induced by an electric motor and transferred to the input shaft followed by an en route to the pinion and wheel of the higher stage. Then, the power is transited from the pinion of the middle stage to the lower stage. The higher and middle stage assembly is made of 20CrMnTi (V-MQ) (GB/T3077) material. Furthermore, a definite kind of six bearings was introduced to connect the casing with the coupled geared system for analyzing the forced and reaction displacement.
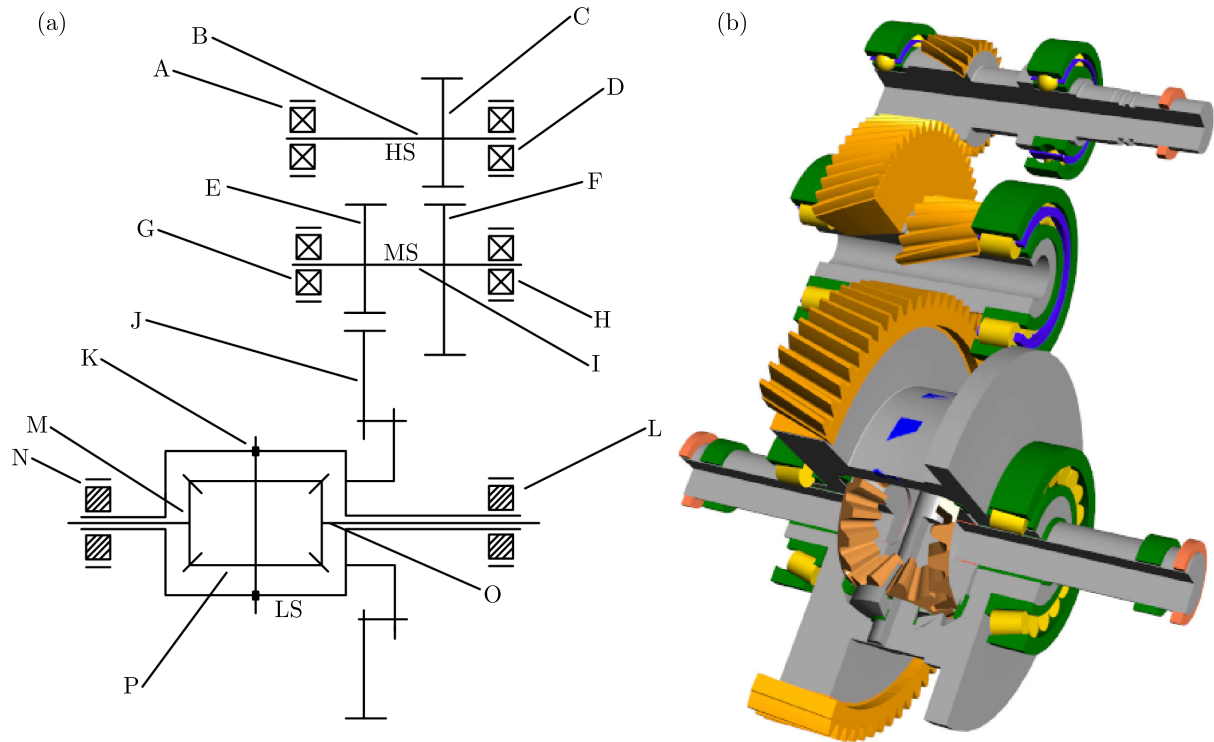
Fig. 2. Gearbox transmission system of an electric vehicle: (a) transmission outline, (b) 3D model in MASTA. Note: HS – higher stage; MS – middle stage; LS – lower stage; A,D – radial ball bearings of the higher stage shaft; B – higher stage shaft; C – pinion of the higher stage; F – wheel of the middle stage; I – middle stage shaft; G,H – radial ball bearings of the middle stage; N,L – taper roller bearings of the lower stage shaft; O,M – half axle gear; P – planet; K – housing of the differential assembly; E – pinion of the middle stage; J – wheel of the lower stage

Table 1. Fundamental geometrical parameters of the differential gearbox

Parameters	Higher stage		Middle stage		Lower stage	
	pinion	wheel	pinion	wheel	planet	sun
No. of teeth	25	60	19	70	10	16
Face width [mm]	27	25	35.5	33	10	10
Module [mm]	2.5	2.5	2.75	2.75	3.75	3.75
Helix angle [°]	22.5	22.5	19	19	–	–
Pressure angle [°]	20	20	20	20	22.5	22.5
Ratio	2.4		3.6		–	

Table 2. Bearing clearance parameters for all stages of the differential gearbox

Stages	Types	Internal radial clearance	Axial clearance
Higher stage shaft	Bearing A,D	$12.5\,\mu\mathrm{m}$	–
Middle stage shaft	Bearing G,H	$12.5\,\mu\mathrm{m}$	–
Lower stage shaft	Bearing N,L	–	$5\,\mu\mathrm{m}$

4. Campbell diagram and critical speed analysis

Campbell diagram is a display of resonance problems, which shows the variation of natural frequencies with rotational speeds. Figures 3 and 4 describe two Campbell diagrams for the first three orders, where speed of rotation [rpm] on the abscissa and frequency [Hz] on the ordinate

are plotted. Moreover, this study is conducted for two different working conditions as presented in Table 3.

Table 3. Load operating parameters for the differential gearbox

	Rated speed	Torque load	Input power load
Condition 1	6000 rev/min	70 Nm	44 kW
Condition 2	12000 rev/min	150 Nm	188 kW

Figure 3 depicts the first three order resonance points of the first working condition for the torque load of 70 Nm. Figure 4 describes the Campbell diagram for the first three orders in the second operating condition for the torque load of 150 Nm.
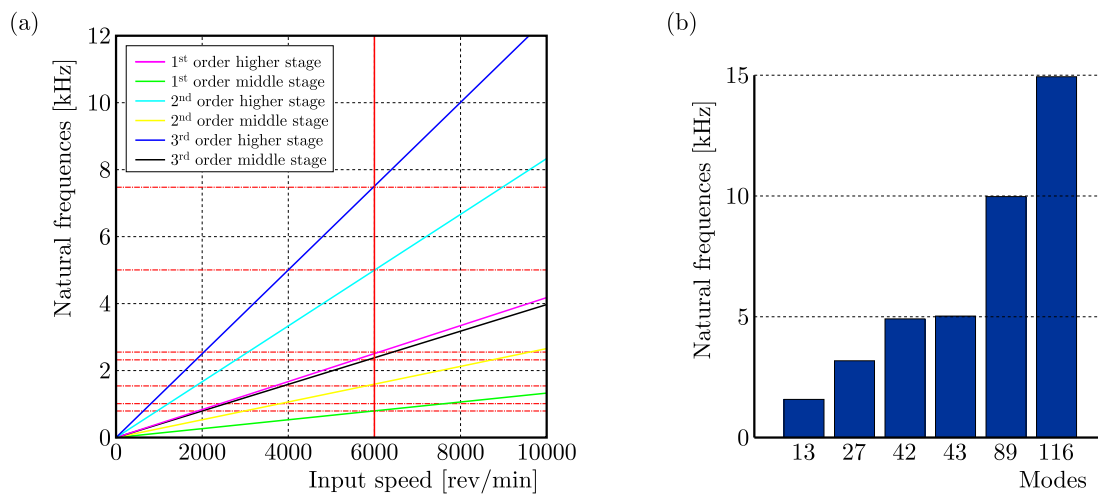
Fig. 3. Campbell diagram and natural frequencies for both stages when the torque load is equal to 70 Nm: (a) Campbell diagram, (b) corresponding modes for the coupled gear sets
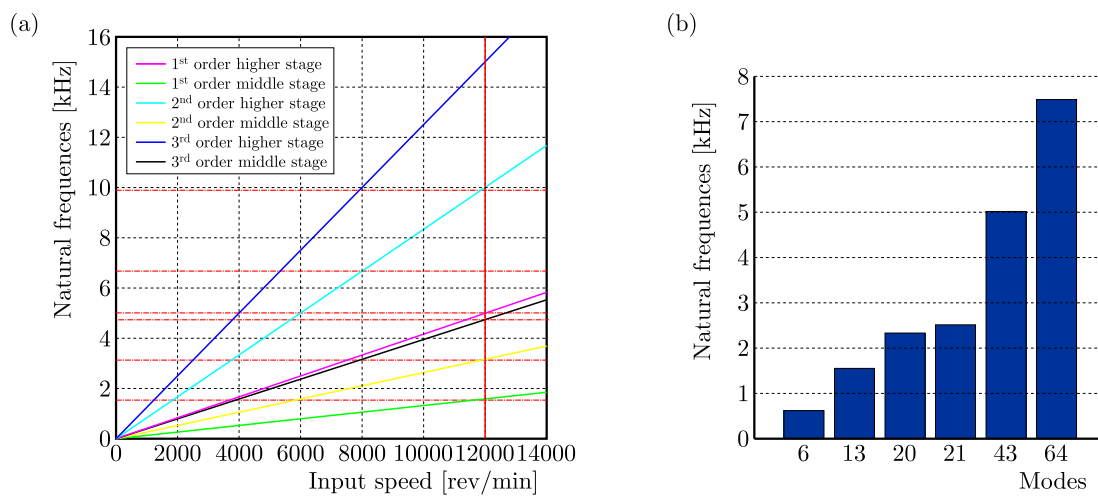

Fig. 4. Campbell diagram and natural frequencies for both stages when the torque load is equal to 150 Nm: (a) Campbell diagram, (b) corresponding modes for the coupled gear sets

5. Dynamic mesh force and resonant modes analysis

This Section simultaneously elaborates the dynamic mesh force and only those critical modes which previously showed the resonance in the Campbell diagram. The dynamic mesh force illustrates how the force acts between two gears in meshing process changes for a variety of frequencies. Thus, the dynamic mesh force was calculated by using a relation between the mesh force and the static transmission error (Harris and Kotzalas, 2006). Then, critical resonance modes were identified for both conditions. Since

$$f = D\delta \tag{5.1}$$

where f is the dynamic mesh force, D is dynamic mesh stiffness and δ stands for transmission error excitation. In addition, the static mesh force was plotted for each gear stage in the case of both working conditions using the following formula

$$F = \frac{P}{d_p w} \tag{5.2}$$

where F and P stand for the static mesh force [N] and rated power [W]; d_p shows the pitch diameter [mm] while w is for the gear set speed [rad/s]. To find the pitch diameter

$$d_P = d_r + m(h_a + c) \tag{5.3}$$

where d_r is the root diameter in mm, m is the normal module while h_a and c present the gear tooth height and modulus coefficient, respectively. By using the aforementioned equations, the static mesh forces came out as 1512N and 5533N for the higher and middle stages for the first rated condition. While 3225.6 N and 11821 N are the static mesh forces for the higher and middle stage, gear pairs for the second condition.
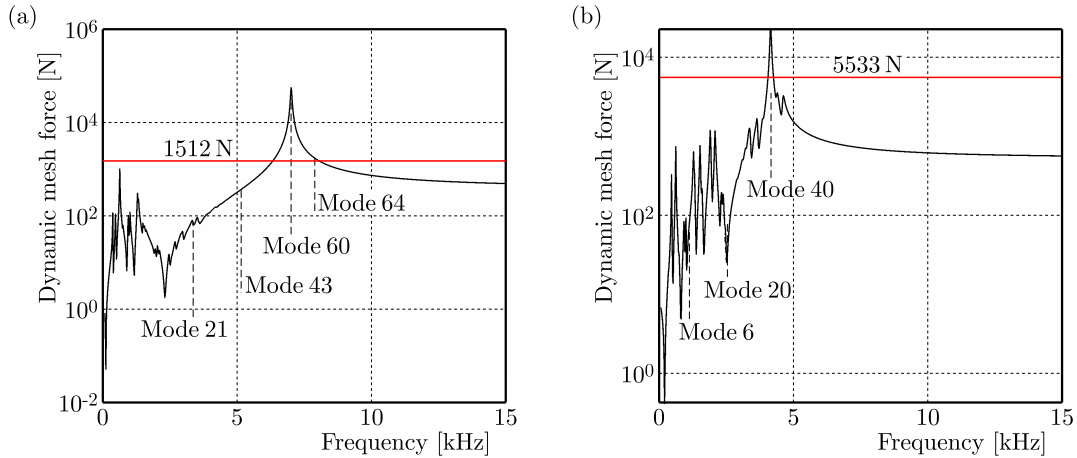

Fig. 5. Dynamic mesh force for both stages when the torque load is equal to 70 Nm: (a) mode orders for higher stage, (b) mode orders for the middle stage

Figure 5 delineates the dynamic mesh force for the torque and rated speed of 70 Nm and 6000 rev/min. Figure 6 shows the dynamic mesh force for both stages in the second condition when the torque and rated speed were 150 Nm and 12000 rev/min, respectively. Thus, the corresponding resonance identification was performed. Hence, the peaks of resonant modes 40, 60 and 64 in Figs. 5 and 6 show that the natural frequencies corresponding to these modes also occur when both the pinion and wheel side compliance curves intersect, they are parallel or close to 180° with each other. Consequently, most of these modes in Figs. 5 and 6 lie in the dangerous zone above the static mesh force showing the possibility of higher vibrations. All other resonant modes, which lie under the static mesh force line in these figures, will not cause unnecessary vibration to the machinery and thus they are safe modes.
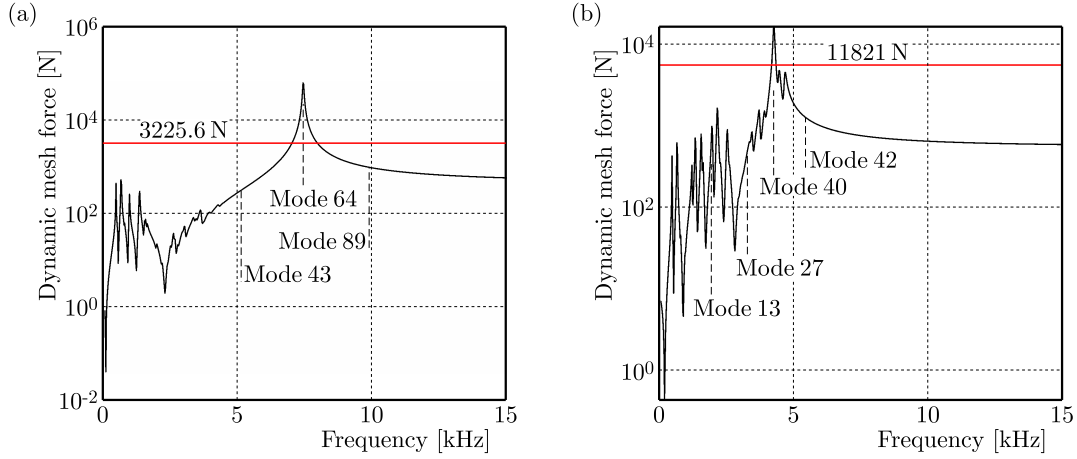
Fig. 6. Dynamic mesh force for both stages when the torque load is equal to 150 Nm: (a) mode orders for the higher stage, (b) mode orders for the middle stage

6. Case studies for mode characteristics analysis

6.1. Parametric influence of bearings internal clearance

To analyze the dynamic mesh force and corresponding resonant modes further, the impact of radial internal clearance in the supporting bearings was analyzed in the first case study. This is done because the corresponding modes can be modified and the resonance can be eliminated by changing the wheel side compliance or pinion side compliance or both. The relationship between the pinion and wheel side compliances is

$$D = \frac{1}{C_p + C_w} \tag{6.1}$$

where C_p and C_w show the pinion and wheel side compliance while D stands for dynamic mesh stiffness.

It is worth mentioning that there are various types of reduction in radial clearances such as clearance reduction due to fit between the outer ring and housing as well as reduction due to fit between the inner ring and shaft. However, the effective bearing radial clearance in this case study was reduced, which is actually the radial distance through which one of the races may be displaced relative to the other, from one eccentric extreme position to the diametrically opposite extreme position. The negative value of the bearing internal clearance ($\Delta = -3$) was also taken due to the fact that the operating clearance turns to be positive by the impact of bearing load. Theoretically, the internal clearance caused by the applied load is given by

$$\Delta_1 = \Delta_0 + \delta_{FO} \tag{6.2}$$

where Δ_1 is the apparent clearance at a specific working load, δ_{FO} is component deformation, Δ_0 is the theoretical radial internal clearance. Generally, the formula for the effective operating internal clearance is presented as

$$\Delta = \Delta_f - \Delta_t \tag{6.3}$$

where Δ_f is the residual clearance after mounting in the shaft and casing. Δ_t shows the clearance reduction due to temperature difference and Δ stands for the operating radial internal clearance.

Figure 7 and 8 are upshots of the first case study for reduced effective internal clearance for both working conditions. As a result of the reduced effective internal clearance, there is a

very minimal decrease in the dynamic mesh force for the higher stage only, but the middle stage dynamic mesh force for the torque load of 150Nm decreased more significantly. It is also evident from Figs. 7 and 8 that the reduction in the effective radial clearance is not so helpful in eliminating resonant modes especially for the higher stage. In short, resonant modes still occur in the analysis results for modes 39, 40, and 60. In other words, dynamic mesh force peaks are appearing, which shows the possibility of vibration for both rated conditions. Hence, it can be inferred that the effective reduced internal clearance does not have a significant impact on the mesh force and resonance elimination.
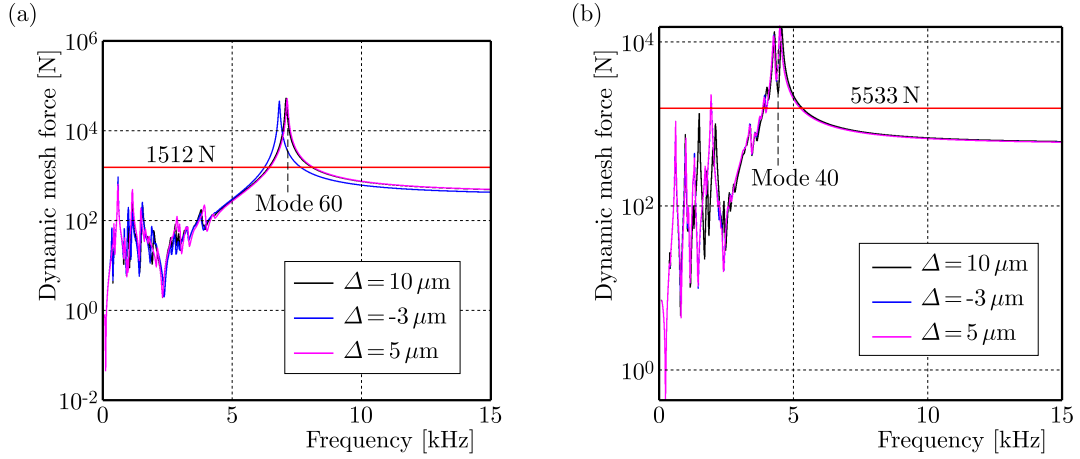

Fig. 7. Effect of the reduced radial clearance on the dynamic mesh force when the torque load is equal to 70 Nm: (a) mode orders for the higher stage, (b) mode orders for the middle stage
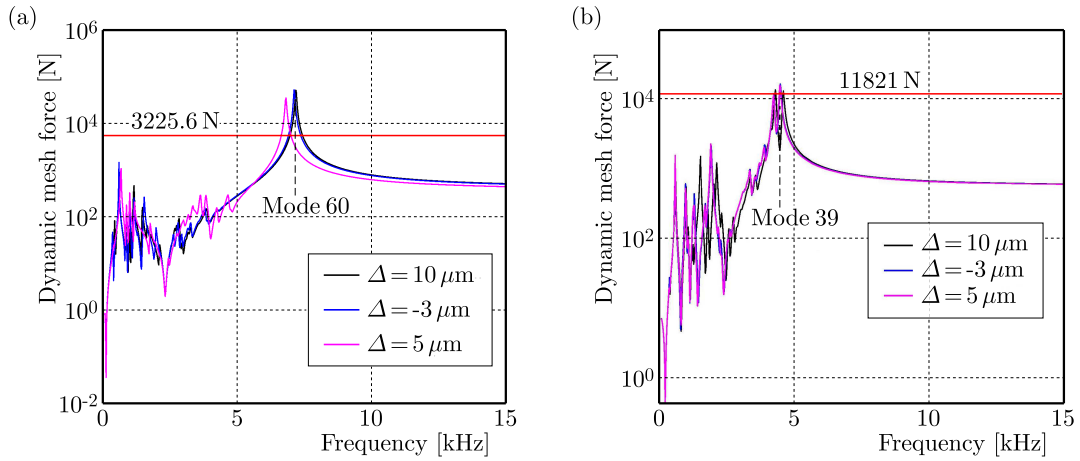

Fig. 8. Effect of the reduced radial clearance on the dynamic mesh force when the torque load is equal to 150 Nm: (a) mode orders for the higher stage, (b) mode orders for the middle stage

6.2. Parametric influence of pinions face width

Face width of pinions of the higher and middle stage gear set was modified in this case study to analyze dynamics of the mesh force by keeping in view the resonant modes. However, at the same time, face width of the wheels of both stages were kept constant. Generally, the relation to face width in the line of action during gear meshing can be represented as

$$b = \frac{F_{\beta_x}}{\tan \Delta} \qquad \Delta = \theta_{skew} \cos \alpha_{\omega t} + \theta_{slope} \qquad (6.4)$$

where F_{β_x} and b are the gear mesh misalignment and face width, respectively; Δ is gear mesh misalignment angle; $\alpha_{\omega t}$ is working pressure angle; θ_{skew} and θ_{slope} present gear skew and gear slope angles, respectively. By using the face width, the gear mesh misalignment can be determined, which could be further used to find the contact face load factor. Theoretically, the contact face load factor can be defined as

$$K_{H\beta} = \frac{\max(F/b)}{F_m/b} \tag{6.5}$$

where $K_{H\beta}$ shows the face load factor; F and F_m stand for the load at an arbitrary position of the tooth flank and the mean (average) load, respectively (Standard and ISO, 2006). The contact face load factor is important in gear strength and design ratings not only for typical but also for special configuration of differential gearboxes. Hence, this approach should be used when the face load factor is equal or greater than 1, so that the optimum strength for gear stages could be maintained.
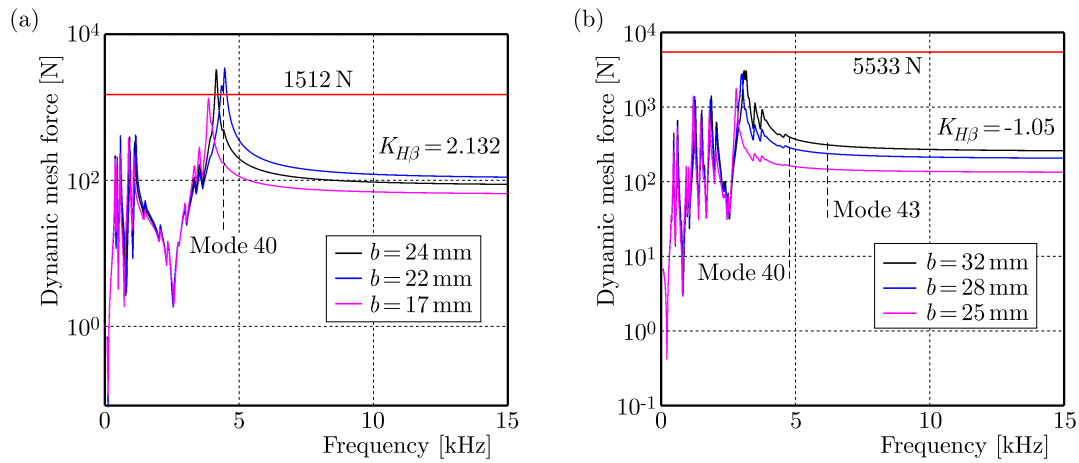

Fig. 9. Effect of the reduced face width on the dynamic mesh force when the torque load is equal to 70 Nm: (a) mode orders for the higher stage, (b) mode orders for the middle stage
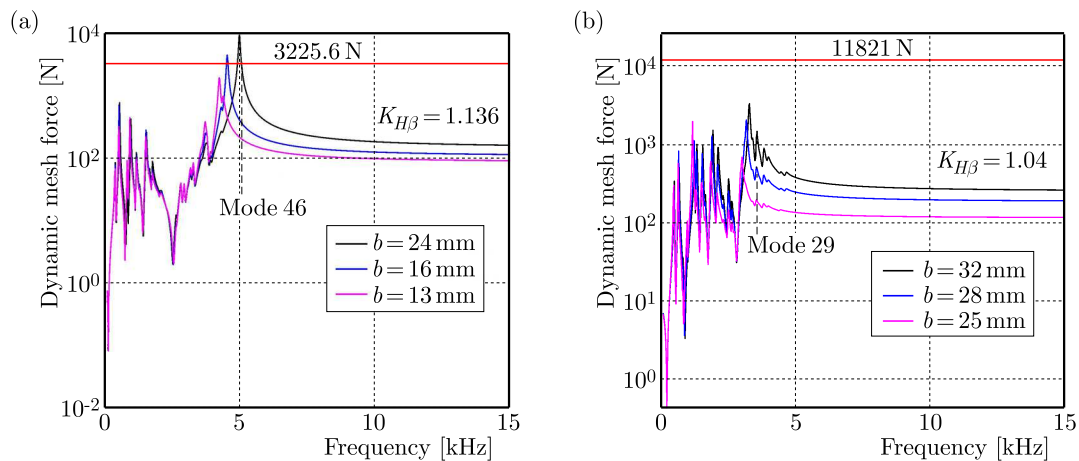

Fig. 10. Effect of the reduced face width on the dynamic mesh force when the torque load is equal to 150 Nm: (a) mode orders for the higher stage, (b) mode orders for the middle stage

Figures 9 and 10 are the outcomes of reduced face width for pinions of the corresponding higher and middle stages, which are analogous to the rated torque loads of 70 Nm and 150 Nm, respectively. As soon as the torque load increases, the impact of reduced face width causes

prompt reduction in the dynamic mesh force and, thus, resonance elimination is more obvious for the higher stage, see Figs. 9a and 10a. However, the most optimum face width was just 17 mm for the higher stage when all the resonant modes fell in the safe region. Yet, various face width of pinions in the middle stage propelled the dynamic mesh force downward and so the corresponding resonant modes were in the safe region, which is apparent from Figs. 9b and 10b. Hence, it can be deduced that reduced face width has a higher impact on the dynamic mesh force and thus it remained more successful in eliminating resonant modes in both working conditions.

7. Concluding remarks

In this study, dynamic modeling is performed for particular configuration of a differential gearbox composed of higher and middle stages by considering the relative displacement and dynamic transmission error. Then, detailed critical modes are investigated by analyzing the Campbell diagram for two operating conditions. For parametric study of the dynamic mesh force and resonant modes, case studies were performed by considering the radial clearance and face width for the first three critical orders. The results show that reduction in radial clearance while maintaining axial clearance for the lower stage as constant remained almost inefficient especially in the higher stage. However, there was nominal resonance elimination in the middle stage under both working conditions. By reducing face width of pinions in the second case study while retaining the face width of wheels as constant proved to be a better approach to resonance elimination and mesh force reduction. Hence, the dynamic mesh force decreased more significantly for both gear stages and most of the corresponding modes fell in the safe region for several parameters. In all case studies, the corresponding modes of the dynamic mesh force for both stages were also prone to shift their location for a variety of natural frequencies.

References

1. ABOUEL-SEOUD S.S., MOHAMED E.S., ABDEL-HAMID A.A., ABDALLAH A.S., 2013, Analytical technique for predicting passenger car gearbox structure noise using vibration response analysis, *British Journal of Applied Science and Technology*, **3**, 4, 860-883

2. CARA J., JUAN J., ALARCÓN E., REYNDERS E., DE ROECK G., 2013, Modal contribution and state space order selection in operational modal analysis, *Mechanical Systems and Signal Processing*, **38**, 276-298, DOI: 10.1016/j.ymssp.2013.03.001

3. CHAVAN D.S., MAHALE A.K., THAKUR A.G., 2013, Modal analysis of power take off gearbox, *International Journal of Emerging Technology and Advanced Engineering*, **3**, 70-76

4. CHEN Z., ZHAI W., WANG K., 2019, Vibration feature evolution of locomotive with tooth root crack propagation of gear transmission system, *Mechanical Systems and Signal Processing*, **115**, 29-44

5. GUO M., LI B., YANG J., LIANG S,, 2015, 1745. Study of experimental modal analysis method of machine tool spindle system, *Journal of Vibroengineering*, **17**, 9, 3173-3186

6. HARRIS T.A., KOTZALAS M.N., 2006, *Rolling Bearing Analysis*, 2 vol, CRC Press

7. KARRAY M., FEKI N., KHABOU M.T., CHAARI F., HADDAR M., 2017, Modal analysis of gearbox transmission system in bucket wheel excavator, *Journal of Theoretical and Applied Mechanics*, **55**, 253-264, DOI: 10.15632/jtam-pl.55.1.253

8. KORKA Z.I., GILLICH N., 2017, Modal analysis of helical gear pairs with various ratios and helix angles, *Romanian Journal of Acoustics and Vibration*, **14**, 91-96

9. KRANJC T., SLAVIČ J., BOLTEŽAR M., 2016, A comparison of strain and classic experimental modal analysis, *Journal of Vibration and Control*, **22**, 371-381

10. KUMAR A., PATIL P.P., 2016, Modal analysis of heavy vehicle truck transmission gearbox housing made from different materials, *Journal of Engineering Science and Technology*, **11**, 252-266

11. LI B., CAI H., MAO X., HUANG J., LUO B., 2013, Estimation of CNC machine-tool dynamic parameters based on random cutting excitation through operational modal analysis, *International Journal of Machine Tools and Manufacture* , **71**, 26-40, DOI: 10.1016/j.ijmachtools.2013.04.001

12. LIU S., SONG C., ZHU C., LIANG C., YANG X., 2019, Investigation on the influence of work holding equipment errors on contact characteristics of face-hobbed hypoid gear, *Mechanism and Machine Theory*, **138**, 95-111

13. LIU W., LIN T.J., PENG Q.C., 2014, Modal analysis and experimental research of marine gearbox, *Applied Mechanics and Materials*, **607**, *Machine Design and Manufacturing Engineering III*, P.S. Wei (Edit.), 405-408

14. LÓPEZ-AENLLE M., BRINCKER R., PELAYO F., FERNANDEZ-CANTELI A., 2012, On exact and approximated formulations for scaling-mode shapes in operational modal analysis by mass and stiffness change, *Journal of Sound and Vibration*, **331**, 622-637, DOI: 10.1016/j.jsv.2011.09.017

15. MAAMAR A., LE T.-P., GAGNOL V., SABOURIN L., 2017, Operational modal analysis of a machine-tool structure during machining operations, *S23-Mécanique des structures*, https://cfm2017.sciencesconf.org/129044/document

16. NENGQUAN D., CAI X., WANG J., 2011, Dynamic characteristics of automobile gearbox of simulation and experimental research, *Cross Strait Quad-Regional Radio Science and Wireless Technology Conference (CSQRWC)*, IEEE, DOI: 10.1109/CSQRWC.2011.6037304

17. Standard, British, and BS ISO, 2006, Calculation of load capacity of spur and helical gears, ISO 6336, 1996

18. WALUNJ P.S., CHOUGULE V.N., MITRA A.C., 2015, Investigation of modal parameters on planetary gearbox using finite element analysis to minimize vibration, *International Journal of Analytical, Experimental and Finite Element Analysis*, **2**, 4, 147-152

19. WU L.-R., XIAO Z.-M., ZHANG H., 2018, Dynamic modeling and modal analysis of RV reducer, [In:] *Innovative techniques and applications of modelling, identification and control*, Zhu Q., Na J., Wu X. (Edit.), Springer

20. YI P., HUANG P., SHI T., 2016, Numerical analysis and experimental investigation of modal properties for the gearbox in wind turbine, *Frontiers of Mechanical Engineering*, **11**, 388-402, DOI: 10.1007/s11465-016-0404-z

21. YU F., LI Y., SUN D., SHEN W., XIA W., 2013, Analysis for the dynamic characteristic of the automobile transmission gearbox, *Research Journal of Applied Sciences, Engineering and Technology*, **5**, 1449-1453

22. ZHOU Q., HAN W., FENG J., JIA X., PENG X., 2017, Numerical simulation and experimental validation of failure caused by vibration of a fan, *IOP Conference Series: Materials Science and Engineering*, IOP Publishing, DOI: 10.1088/1757-899x/232/1/012082